Research Article Vol. 33, No. 3 / 10 Feb 2025 / Optics Express 4604
Optics EXPRESS

Efficient modeling and optimization approach for grating-based flow cytometers

ADAM BARZANJI,[1,2,*] THIJS ULLRICK,[1,3] KRISTOF COOLS,[3] TOM REEP,[1,2] NIELS VERELLEN,[2] GÜNAY YURTSEVER,[2] AND WIM BOGAERTS[1,2]

[1]Photonics Research Group, INTEC, Ghent University - imec, 9052 Ghent, Belgium
[2]IMEC, Kapeldreef 75, 3001 Heverlee, Belgium
[3]IDLab, INTEC, Ghent University - imec, 9052 Ghent, Belgium
[*]adam.barzanji@ugent.be

Abstract: This work presents a computationally efficient transmission matrix model and optimization scheme for the design of silicon nitride grating couplers in integrated scattering-based flow cytometry systems. The proposed model accurately simulates the optical power flow through the grating coupler and microfluidic channel system, enabling precise evaluation of the transient associated with a polystyrene bead's passage through the channel. The transmission matrix model yields a four to five orders-of-magnitude improvement in computational efficiency compared to a finite difference time domain solver, making it suitable for optimization loops consisting of many iterations and objective function evaluations. The model's computational speed is leveraged to quickly simulate the effect of variations in bead dimensions or position in the channel. The model is incorporated into a Bayesian optimization scheme that maximizes the peak to baseline height of the transient by tuning the parameters of both uniform and linearly apodized grating configurations. Results demonstrate a linearly apodized grating configuration, optimized for a dynamic system, yields a 2.49 dB improvement in peak to baseline transmission on the best uniform grating configuration, optimized for a static system.

© 2025 Optica Publishing Group under the terms of the Optica Open Access Publishing Agreement

1. Introduction

1.1. Flow cytometry

Flow cytometry is a critical tool in biomedical research and clinical diagnostics, enabling multi-parameter analysis of cells and particles for classification or sorting. Traditional flow cytometers rely on complex optical systems and often require fluorescent labeling, making them expensive, bulky, and challenging to use in point-of-care or resource-limited settings [1]. In response to these limitations, microfluidic flow cytometry has emerged as a promising alternative, leveraging advancements in microfabrication and electronic integration to create smaller, more cost-effective, and portable devices. These systems can reduce both size and cost, while leveraging parallel processing across multiple channels to enable high cell throughput, but often rely on the sensitive manual alignment of optics with the microfluidic channel [2–4].

Integrated optofluidic systems [5–9], circumvent fiber-channel alignment with integrated planar waveguides that transport light to and from the microfluidic channel, yielding better robustness and fabrication scaling. Fluorescence-based integrated flow cytometers, such as the system presented by Hong *et al.* [10], achieve high classification accuracy but require fluorescent labeling of sample cells prior to analysis. This labeling process can stress cells and adds additional complexity, which may limit suitability for high-throughput applications. Scattering-based integrated flow cytometers offer a promising alternative, as they do not require fluorescent labeling. Recently, Jooken *et al.* [11] demonstrated the first monolithically integrated microfluidic flow cytometry

#547368 https://doi.org/10.1364/OE.547368
Journal © 2025 Received 12 Nov 2024; revised 10 Jan 2025; accepted 18 Jan 2025; published 29 Jan 2025

Optics EXPRESS

system with sufficient resolution for the discrimination of lymphocytes and monocytes, white bloods cells of particular importance in cell therapy, using scattering rather than fluorescence.

However, further optimization is necessary to enhance sensitivity, throughput, and ease of operation, particularly in cell therapy applications where large-scale, high-precision processing of cells, such as lymphocytes and monocytes, is essential. One of the primary factors limiting the sensitivity of integrated systems is the ability of integrated photonic waveguides to efficiently capture optical power. Grating couplers, which are periodic variations in a waveguide's refractive index, enable efficient coupling of light into and out of the waveguide at specific angles and are widely used in integrated photonics to improve power coupling efficiency [12]. This work introduces a computationally efficient approach to modeling the flow of optical power through an integrated grating coupler based microfluidic flow cytometry system such as that proposed by Jooken *et al.* [11] for the discrimination of monocytes and lymphocytes. The model is incorporated into an optimization scheme to maximize collection efficiency and cell detection sensitivity. The result is an optimized grating configuration that offers a substantial improvement in optical power coupling efficiency and cell detection sensitivity compared to the configurations possible using the approach outlined in [11].

1.2. System configuration

The system considered in this work consists of a 30 μm thick microfluidic channel that sits between Si_3N_4-on-oxide photonic waveguides as depicted in Fig. 1 and 2. The detailed stack information is presented in the Sec. 2 of Supplement 1. An Illumination Grating (ILG) and Forward Scattering Grating (FSG) are fully etched into the bottom and top Si_3N_4 waveguides respectively. When the bottom Si_3N_4 waveguide mode is excited from the left with a 638 nm source laser, the ILG scatters light across the microfluidic channel as in Fig. 2. The light then couples into the right propagating mode of the top Si_3N_4 waveguide via the FSG, after which the optical power is edge coupled to fiber optics for downstream processing. In an Axial Light Loss (ALL) mode [11,13], the primary diffraction lobe of the ILG is directed towards the FSG. The static mode-to-mode power transmission through the system forms the baseline signal for cell detection events.

A R_{bead} = 3 μm radius spherical polystyrene bead, representing a monocyte or lymphocyte, travels through the microfluidic channel. When the bead passes through the ILG light, it scatters light away from the FSG as in Fig. 3. As a result, less optical power couples into the FSG output waveguide and a transient dip in the power transmission is observed. The difference between the peak minimum FSG power transmission, and the respective baseline transmission will henceforth be called the Peak to Baseline (**P2B**) and used as a metric for cell detection sensitivity and characterisation. This metric has been used in other work [11] and is analogous to the "Pulse Height" metric traditionally used in flow cytometry.

1.3. Polystyrene bead

A polystyrene bead exhibits high orientational symmetry due to its spherical shape, meaning its optical properties are invariant under rotation. When cells are freely suspended in a quiescent fluid, they tend to adopt a nearly spherical shape. This default spherical shape is favored because, in the absence of other forces, the cell's cytoskeleton and membrane tension minimize surface area for a given volume [14]. However, once these cells are subjected to flow—particularly in confined microfluidic channels—several factors influence their morphology. As the shear rate increases, especially in channels on the order of the cell's diameter, cells may elongate or flatten along the direction of flow. Meanwhile, the presence of a large, relatively rigid nucleus [15] in most white blood cells can limit deformation compared to anuclear cells (e.g., red blood cells or platelets). Furthermore, activated T cells often become stiffer or change shape differently than resting cells, which can further alter their response to shear [16]. Consequently, these

Optics EXPRESS

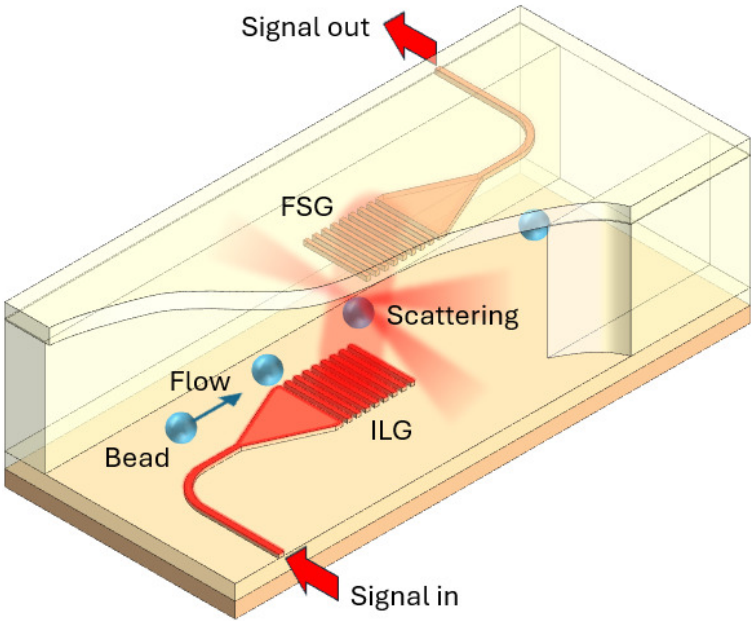

Fig. 1. 3D schematic of microfluidic system depicting optical power flow from the ILG to the FSG and the scattering of light caused by the bead's passage through the channel.

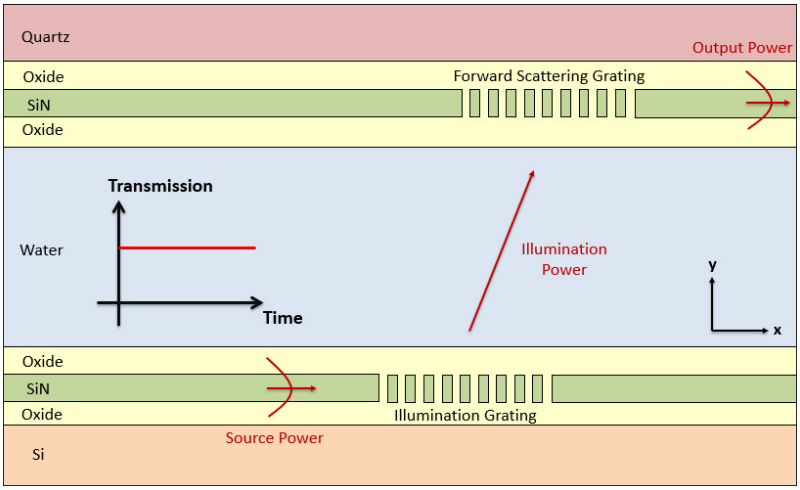

Fig. 2. 2D Schematic of the static system power flow, an ALL configuration where the scattered optical power from ILG is directed towards the FSG. The static transmission is a baseline for detection events.

Optics EXPRESS

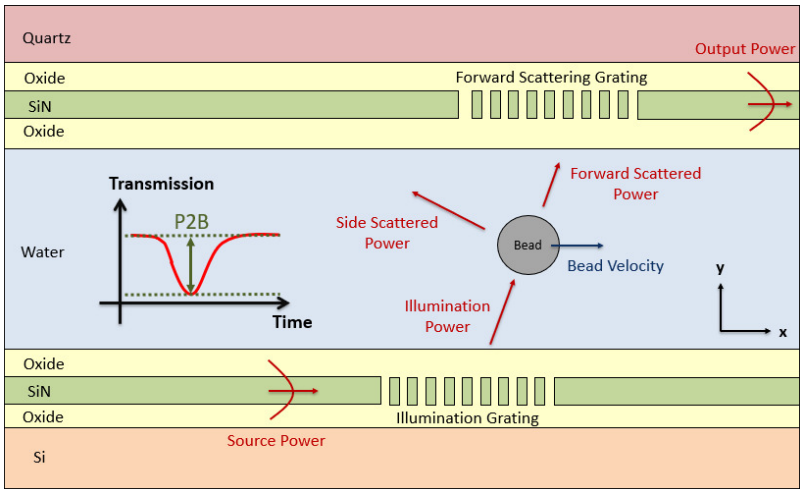

Fig. 3. Schematic of the dynamic system power flow when a bead travels through the channel. The Peak To Baseline (P2B) of the transient dip in power transmission, induced by the bead's passage through the channel, is the metric for cell detection in this work.

factors introduce orientational asymmetries in cell shape, breaking the optical uniformity seen in simple spherical objects. Thus, the utility of a polystyrene bead in flow cytometry modeling is constrained by its inherent spherical symmetry. It may not accurately mimic the optical behavior of, for instance, an ellipsoidal cell. However, Jooken et. al. [11] demonstrate that a polystyrene bead is a sufficient surrogate to meaningfully model and optimize the proposed system for the discrimination of monocytes and lymphocytes. Furthermore, while the model for the bead in this work assumes spherical symmetry, a strategy to incorporate arbitrary bead geometries in the modeling scheme is discussed in Section 3.2.

1.4. Modeling and optimization objectives

From [11] we can assume that P2B in ALL mode increases with bead size up to a saturation point. Consequently, the difference in P2B between beads of different sizes, $\mathbf{\Delta P2B_{\Delta R}}$, similarly increases with increasing bead size. By optimizing the P2B for a bead of a given size, e.g., R_{bead} = 3 μm, we implicitly optimize $\Delta P2B_{\Delta R}$. Since a larger $\Delta P2B_{\Delta R}$ enables better cell discrimination, the grating configuration will be optimized for maximal P2B.

As such, from a photonic perspective, the objective is to design the ILG and FSG, in particular their relative position and geometry, for a maximal P2B, resulting in improved bead detection sensitivity and discrimination. While one might intuitively assume that maximizing baseline transmission would also maximize P2B, this is not necessarily guaranteed. Achieving this optimization requires a method for efficiently and accurately simulating transients so that P2B may be computed for a given grating configuration. This, in turn, necessitates an accurate model of optical power flow from the excitation laser through the system to the FSG output as the bead moves through the channel.

Therefore, the objectives of this paper are twofold:

1. Accurately model and simulate optical power transmission through both a static system consisting of an empty channel and a dynamic system, where a bead passes through the channel.

2. Integrate the model into an appropriate optimization scheme that adjusts the relative position and geometry of the gratings to achieve a configuration that maximizes P2B.

Optics EXPRESS

This work presents a 2D model of the system, treating the spherical polystyrene bead as a 2D lossless dielectric cylinder. While a 2D model does not account for effects arising from a positional offset of the bead along the z-axis, nor does it model any polarization mixing induced by a spherical dielectric, it should still capture sufficient system behavior to meaningfully optimize the gratings, provided the gratings are sufficiently wide along the z-axis, relative to the bead's radius. The microfluidic channel will be approximated as a static, homogeneous dielectric, with dynamics and inhomogeneity caused by effects such as turbulence not modeled in this work. This work will model and optimize uniform period or linearly apodized parameterizations of fully etched ILG and FSG.

1.5. Computational efficiency

A straightforward approach to modeling the mode-to-mode power transmission through an inter-layer grating system is to simulate the entire system using Finite Element Method (FEM) or Finite Difference Time Domain (FDTD) packages such as the commercially available COMSOL Wave Optics or Ansys Lumerical FDTD [11,17,18]. However, the 30 μm thickness of the microfluidic channel, depicted in Fig. 2, results in a relatively large simulation space which adds substantial computational overhead to simulate a largely geometrically featureless region. For a static, empty channel, inverse design tools such as the Lumerical library lumopt [19] might be used to optimize the grating configuration and maximize mode-to-mode power transmission. Such tools leverage the adjoint method and have been widely adopted for the optimization of grating couplers [20–23]. However, in addition to the computational overhead of FDTD simulations, these tools do not allow the simulation of transients associated with a dynamical system as in Fig. 3, but instead, only facilitate mode-to-mode transmission optimization of a static system such as in Fig. 2.

The inclusion of a dielectric cylinder in the channel might suggest the use of an FDTD or FEM-based approach, which can accommodate rounded geometries. However, to compute the transient transmission P2B, the x position of the bead would be swept in discrete steps through the channel, with mode-to-mode transmission simulated at each position. As a result, the computation of the transient transmission P2B would necessitate numerous computationally intensive FDTD or FEM simulations for a single grating configuration, leading to an excessively high computational cost. This cost can be mitigated by increasing the step size when translating the bead or by reducing the FDTD or FEM mesh refinement, but such adjustments would compromise the accuracy of the transient and P2B computations. An optimization loop requiring an extensive amount of P2B calculations would further compound the overall computational cost, making the optimization process prohibitively time-consuming.

To address these limitations, this work presents a computationally efficient method to accurately model the system transient, which is several orders of magnitude faster than an FDTD, leading to faster and computationally less expensive optimizations. To assess and validate the accuracy of the proposed method, Lumerical FDTD simulation sweeps are utilized as a reference benchmark.

For grating parameterizations with only 2 variables, such as period and relative position, a brute-force grid search approach adopting large sweep steps can be used to obtain an approximate optimal grating configuration within a reasonable time frame. However, when considering higher precision or a higher-dimensional input space, by e.g. incorporating a linear apodization of the grating profile, an effective and reliable optimization scheme is crucial for determining the optimal solution. To this end, Bayesian Optimization (BO) is selected in this work to optimize the system configuration, enabling a more efficient search of the parameter space with fewer objective function evaluations and no hyper-parameter tuning compared to Particle Swarm or Genetic Algorithms [24].

Optics EXPRESS

2. Static system

2.1. Model outline

The first objective is to model the power transmission in a static system, from the excitation to the FSG output. To simplify the analysis the following observations of the system can be made:

1. The scattering system consists of only passive, linear components i.e. waveguides, grating couplers, a dielectric bead and a microfluidic channel which can be modeled with lossless dielectric media.
2. The optical transmission is problem of mode to mode coupling involving only a single wavelength i.e. 638 nm.
3. The scattering system is comprised of reciprocal components i.e. light transmission is reversible.

Due to the system's linearity, it can be decomposed into a number of modular sub-components and perform a Transmission Matrix Model (TMM) and Angular Spectrum Method based analysis [25,26]. The components of these transmission matrices are the transmission characteristics of plane waves $\mathbf{a_i}$ in Fig. 4 emerging from the gratings at different angles. The empty channel system, depicted in Fig. 4, can be represented by the matrices:

1. $\mathbf{t}_{A\to B}$ transmission from the guided mode of the input waveguide (A) to the plane waves at the bottom of the microfluidic channel (B) for a given ILG geometry
2. $\mathbf{t}_{B\to C}$ transmission of plane waves propagating from the bottom (B) to the top (C) of microfluidic channel
3. $\mathbf{t}_{C\to D}$ transmission of the plane waves at the top of the microfluidic channel (C) to the guided mode of the output waveguide (D) for a given FSG geometry

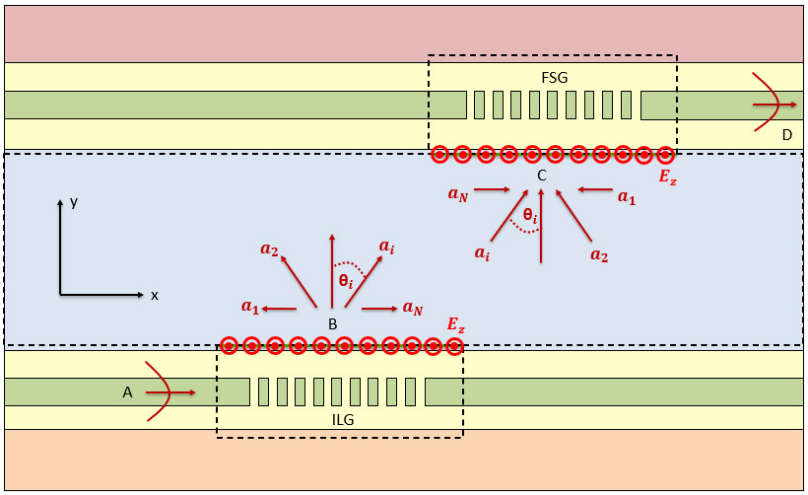

Fig. 4. TMM modularization of the static system via decomposition of grating fields $\mathbf{E_z}$ into plane waves of amplitudes $\mathbf{a_i}$ propagating at an angle $\theta_\mathbf{i}$. Static modal coupling from A to D is calculated by cascading the ILG, microfludic channel and FSG matrices resulting from this TMM modularization.

Cascading the transmission matrices of the sub-components between the input waveguide and the output waveguide simulates the modal flow through these sub components such that the

Optics EXPRESS

input to output power coupling may be calculated via Eqn. (1). Using an FDTD to simulate the broadband fields throughout the entire system, which primarily consists of a uniform microfluidic channel, adds unnecessary computational overhead since we are only interested in mode to mode coupling at a single wavelength. The problem is instead reduced to calculating the fields above the gratings, performing a plane wave decomposition of these fields followed by the multiplication of a small number of matrices. Such numerical operations can be efficiently implemented in Python and are several orders of magnitude faster than an FDTD simulation of the complete system. The plane wave decomposition will only include upward propagating waves, disregarding any downward or back-scattered waves. Given the substantial thickness of the channel, fields reflected within it would disperse significantly before reaching and coupling to the FSG. Therefore, their contribution to mode-to-mode transmission is negligible and it is a reasonable approximation to discard downward propagating or back-scattered waves.

$$T_{A\to D} = |t_{A\to D}|^2 = |\mathbf{t}_{C\to D} \cdot \mathbf{t}_{B\to C} \cdot \mathbf{t}_{A\to B}|^2 \tag{1}$$

2.2. Illumination grating

The transmission matrix $\mathbf{t_{A->B}}$ for a given ILG geometry may be found by first calculating the z-polarized electric fields above the grating (B) when the z polarized guided mode of the input waveguide (A) is used as an excitation see, Fig. 4. A Discrete Fourier Transform (DFT) is then applied to the fields to extract a discrete angular plane wave spectrum and populate the elements of $\mathbf{t_{A->B}}$. The fields are simulated using Cavity Modeling Framework (CAMFR) [27], an eigenmode expansion package with a Python interface. For a relatively large but simple stack of uniform layers such as in Table S1 of Supplement 1, CAMFR first computes the stack eigenmodes and inter-layer coupling to efficiently evaluate the electric fields at a given number of points above the grating for a single-wavelength guided mode excitation. This computation could alternatively be performed by an FDTD solver to compare its efficiency with CAMFR, as in Sec. 5.C. of Supplement 1. However, an FDTD computes broadband fields throughout the large slabs of the ILG with a sufficiently discretized mesh. Since the objective is to compute fields of a single wavelength through the geometrically simple slabs of the ILG, an FDTD solver potentially adds unnecessary computational overhead. Table S2 of Supplement 1 supports this and consequently the FDTD solver is reserved for validation.

The DFT in Eqn. (2) is then applied to the $M = 300$ sample field points at positions x_m computed by CAMFR, to extract each plane wave a_i of angle θ_i, or equivalently angular bin $\Delta\theta_i$, for N upward propagating plane waves between $-90° \le \Delta\theta_i \le 90°$ schematically represented in Fig. 4. Examples of plane wave transmission spectra for different periods are found in Fig. S3 of Supplement 1.

$$a_i[\Delta\theta_i] = \frac{E_z[\Delta\theta_i]}{\sqrt{\eta_w}} = \sqrt{\frac{\Delta k_i}{2\pi\eta_w}} \sum_{m=0}^{M} E_z[x_m] e^{j\Delta k_i \cdot x_m} \tag{2}$$

In Eqn. (2), $\eta_w = 284\,\Omega$ is the electromagnetic impedance of the water channel. The wavenumber bin widths Δk_i used in in Eqn. (2) were chirped by Eqn. (3), to maintain equal angular bin $\Delta\theta_i$ widths. In Eqn. (3) λ_0 is the free space wavelength and n_w is the corresponding the refractive index of water 1.33. While the method described in this work can be applied to any wavelength, all the simulations presented in this work assume a free space wavelength of 638 nm. Equal angular bin widths are both notationally convenient and, as demonstrated in Sec. 7 of Supplement 1, simplify the construction of the transmission matrix $\mathbf{t}_P$ of a bead with circular symmetry.

$$\Delta k_i = \frac{2\pi n_w}{\lambda_0} sin(\Delta\theta_i) \tag{3}$$

For a unity power input guided mode, the plane wave components found using Eqn. (2) populate the entries of the ILG transmission matrix $\mathbf{t_{A->B}}$ in Eqn. (4). As such, $\mathbf{t_{A->B}}$ represents

Optics EXPRESS

the discrete angular transmission spectrum for upwards propagating plane waves traveling at an angle of $-90° \leq \Delta\theta_i \leq 90°$ to the normal.

$$\mathbf{t}_{A\to B} = \begin{pmatrix} t^{(1)}_{A\to B} \\ \vdots \\ t^{(N)}_{A\to B} \end{pmatrix} = \begin{pmatrix} a_1 \\ \vdots \\ a_N \end{pmatrix} \tag{4}$$

2.3. Microfluidic channel

The empty microfluidic channel may be considered a lossless, uniform, dielectric medium. A plane wave $\mathbf{a}_i$ propagating through a lossless dielectric undergoes a phase rotation ϕ_i given by the dot product, Eqn. (5) [26], of the plane wave's k_i and the distance traversed by the plane wave r_1, depicted in Fig. 5.

$$\phi_i = \boldsymbol{k_i} \cdot \boldsymbol{r_1} = \frac{2\pi n_w}{\lambda_0}\sqrt{x_1^2 + y_1^2}cos(\theta_i - \alpha_1) \tag{5}$$

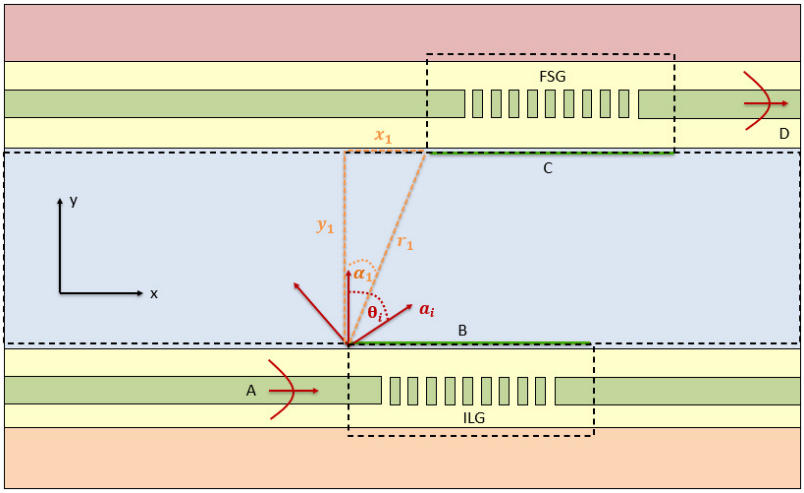

Fig. 5. System schematic depicting plane wave a_i with propagation angle θ_i and the distance traversed by the plane wave through the microfluidic channel r_1 (composed of x_1 and y_1) at an angle α_1. These parameters are used to determine the plane wave phase rotations by Eqn. (6) used in the construction of the empty microfluidic channel transmission matrix in Eqn. (7).

Consequently, each plane wave in a discrete transmission spectrum such as $\mathbf{t_{A->B}}$ undergoes a different phase rotation as they traverse the same displacement $\mathbf{r_1}$. The phase rotation for each plane wave in $\mathbf{t_{A->B}}$ is used to calculate its respective transmission by Eqn. (6) which is then used to populate the transmission matrix $\mathbf{t_{B->C}}$ in Eqn. (7).

$$t^{(i)}_{B\to C} = e^{-j\phi_i} \tag{6}$$

$$\mathbf{t}_{B\to C} = \begin{pmatrix} t^{(1)}_{B\to C} & \cdots & 0 \\ \vdots & \ddots & \vdots \\ 0 & \cdots & t^{(N)}_{B\to C} \end{pmatrix} \tag{7}$$

In this scheme, spatially translating the endpoint of $\mathbf{r_1}$ e.g. moving the endpoint from $x_1 = 0\mu m$ to $x_1 = 5\mu m$ or $x_1 = 10\mu m$ is equivalent to regenerating $\mathbf{t_{B->C}}$ with a new set of phase rotations

Optics EXPRESS

for each angular spectrum component such as in Fig. 6. The advantage of this scheme is that spatially translating a sub-component with a fixed transmission matrix, such as a grating or bead, becomes a simple and fast operation in contrast to re-simulating fields throughout the entire system in an FDTD when a sub-component is translated.

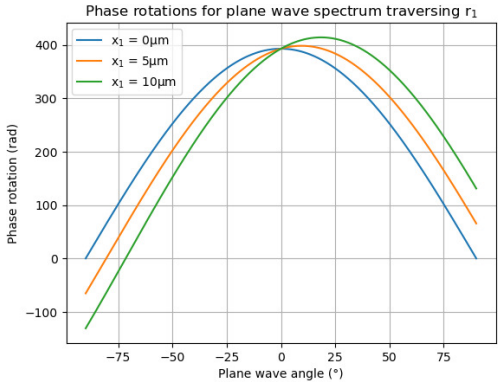

Fig. 6. Phase rotations applied to a plane wave spectrum with propagation angles $-90^\circ \leq \Delta\theta_i \leq 90^\circ$ caused by translation along r_1 for $x_1 = 0\mu m, 5\mu m, 10\mu m$. The FSG or bead position in the TMM is fixed by populating $\mathbf{t_{B->C}}$ in Eqn. (7) with the appropriate set of phase rotations.

2.4. Forward scattering grating

The transmission matrix of the FSG $\mathbf{t_{C->D}}$ was found by the same procedure as the ILG but three additional steps are performed and described in more detail in Sec. 4 of Supplement 1. First, a 180° rotational transformation, $\mathbf{R_{180^\circ}}$ in Eqn. (8) orients the grating as it appears in the system and in Fig. S7 of Supplement 1, applying a 180° rotation of the angular spectrum. Second, the reciprocity theorem dictates that the transmission of the waveguide mode to the scattered fields may be reversed by Hermitian conjugation, yielding the desired transmission direction as in Eqn. (8). Finally, the FSG is horizontally translated to the desired zero position.

$$\mathbf{t}_{C\to D} = \begin{pmatrix} t^{(1)}_{C\to D} & \cdots & t^{(N)}_{C\to D} \end{pmatrix} = \mathbf{R_{180^\circ}} \begin{pmatrix} t^{(1)}_{D\to C} \\ \vdots \\ t^{(N)}_{D\to C} \end{pmatrix}^H \tag{8}$$

2.5. Model validation and benchmarking

For a given grating configuration, the sub-component matrices $\mathbf{t_{A->B}}$, $\mathbf{t_{B->C}}$ and $\mathbf{t_{C->D}}$ may now be found and used to evaluate the static mode to mode power transmission $T_{A->D}$ via Eqn. (1). The performance of the model may be validated by comparing its output and computational runtime with an FDTD reference simulation. In this approach, ILG and FSG's with equal periods $\Lambda = 0.49$ μm were defined in both the TMM and Lumerical FDTD and the mode to mode power transmission was calculated while sweeping the x position of the FSG from −10 μm to 10 μm. While $\Lambda_{ILG} = \Lambda_{FSG} = 0.49$ μm was chosen for the validation and benchmarking, the choice is not critical and any grating period could have been used. The sweep results for 21-period and 41-period gratings provided in Fig. 7 demonstrate excellent agreement between the TMM and FDTD methods. The transmission profiles exhibit a very similar shape, showing coinciding peaks and small transmission errors across the sweep range.

Optics EXPRESS

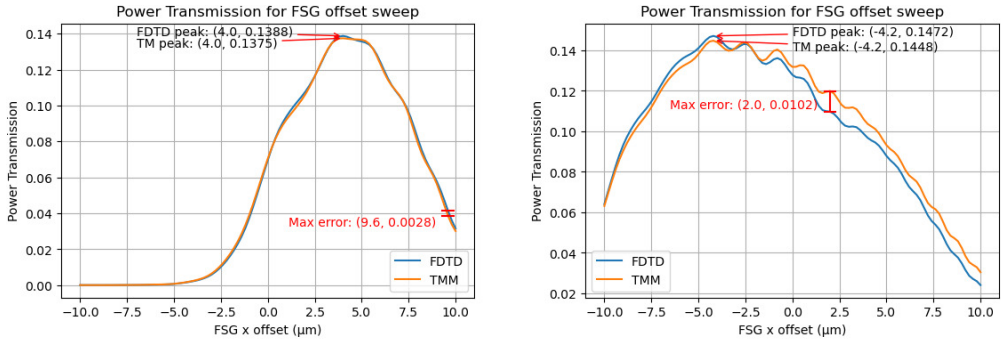

(a) Grating with 21 periods.

(b) Grating with 41 periods.

Fig. 7. Power transmission calculated while sweeping FSG horizontal offset x_{FSG} by both a 2881 plane wave TMM and Lumerical FDTD for grating periods of $\Lambda_{ILG} = \Lambda_{FSG} = 0.49$ μm. The similar shape, coinciding peaks and small transmission errors indicate close agreement between the TMM and FDTD simulations.

The TMM does not take into account plane wave reflection between the ILG and FSG stacks. As the period count increases, optical power scattered by the ILG, and consequently optical power reflected between the ILG and FSG stacks increases. While for a 30 μm channel thickness this effect would be small, it potentially accounts for the slightly larger transmission error in the case of the longer, 41-period grating. The FDTD convergence analysis outlined in Sec. 5.B. of Supplement 1, shows that the FDTD results do not perfectly converge for a 41-period grating even at the highest mesh accuracy setting. This introduces an additional source of error that may contribute to the difference in transmission characteristics. Nonetheless, the TMM for a static system produces results that are sufficiently close to those of FDTD simulations, validating its accuracy. Table 1 compares the total computation times for the sweeps in Fig. 7. A single full FDTD simulation in Ansys Lumerical FDTD, using an automatic non-uniform mesh, takes on average 840 s (see Fig. S12 of Supplement 1) and 5109 s (see Fig. S13 of Supplement 1). To estimate the total sweep computation time for the FDTD, the average is multiplied by the number of positions in the sweep (101 positions). This represents a 4 to 5 orders of magnitude improvement in computational runtime, demonstrating the power of the TMM. The computation time of the TMM is dominated by the grating field calculations in CAMFR, rather than the transmission matrix multiplications. As such increasing the sweep length or resolution negligibly affects the computation time of the TMM. Conversely, increasing the sweep length or resolution would significantly ramp up the total computation time for the FDTD model.

Table 1. Computation times of the 101 point static x_{FSG} sweeps in Fig. 7 performed on the same computational hardware.

Periods	Model	Computation Time (s)
21	FDTD	8.48×10^4
21	TMM	15
41	FDTD	5.16×10^5
41	TMM	50

Optics EXPRESS

2.6. Grid search

The model can be utilized to effectively compute the static transmission on a uniform grid by sweeping the grating period in 201 steps of 1 nm from 0.4 μm to 0.6 μm, and the FSG offset across 201 steps of 10 nm between −5 μm and 15 μm. The results of this sweep are shown in Fig. 8. Little power coupling is observed below 0.42 μm, where a significant portion of the excitation power is back-reflected within the waveguide rather than radiated. A maximum static transmission of $T_{max} = 0.1374$ is obtained with grating periods of $\Lambda_{ILG} = \Lambda_{FSG} = 0.510$ μm and a FSG offset of $x_{FSG} = 5.30$ μm for gratings with 20 periods. The brute-force grid search using the TMM method took the TMM approximately 54 minutes to complete. Considering FDTD simulations with a computational runtime of roughly 14 minutes per grating configuration, we can predict that the grid search shown in Fig. 8 would take approximately $201 \times 201 \times 14$ min ≈ 392 days on the same computational hardware.

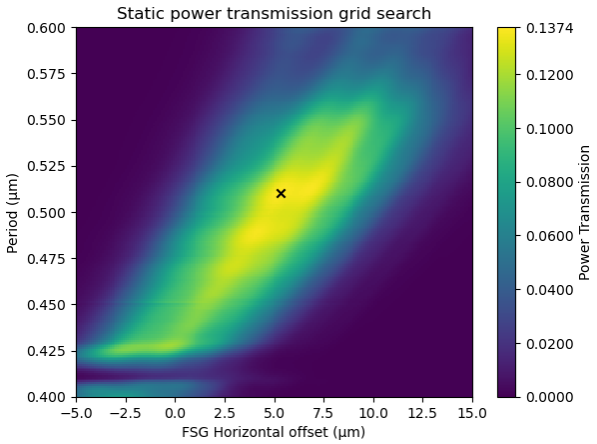

Fig. 8. Static power transmission calculation, sweeping $\Lambda_{ILG} = \Lambda_{FSG}$ (for a 20-period grating) and the FSG horizontal offset x_{FSG}. The maximum static power transmission is $T_{max} = 0.1374$ obtained with $\Lambda_{ILG} = \Lambda_{FSG} = 0.510$ μm and $x_{FSG} = 6.1$ μm and indicated on the heat map with a black cross.

3. Dynamic system

3.1. Model outline

With the TMM for the static system validated, the model may be expanded to a dynamic system where a polystyrene bead passes through the microfluidic channel. Placing a bead in the channel replaces the $\mathbf{t}_{B\to C}$ matrix with 3 matrices such that the input to output power transmission may be described by Eqn. (9):

1. $\mathbf{t}_{B\to P}$ transmission of plane waves, $\mathbf{a_i}$ in Fig. 9 propagating from the bottom (B) of microfluidic channel to the center of the bead (P)
2. $\mathbf{t}_P$ the scattering of plane waves by the bead (P), a dielectric cylinder in 2D
3. $\mathbf{t}_{P\to C}$ transmission of the plane waves $\mathbf{a_s}$ in Fig. 9 scattered by the bead (P) propagating to the top of the microfluidic channel (C)

$$T_{A\to D} = |t_{A\to D}|^2 = |\mathbf{t}_{C\to D}.\mathbf{t}_{P\to C}.\mathbf{t}_P.\mathbf{t}_{B\to P}.\mathbf{t}_{A\to B}|^2 \tag{9}$$

For a bead of a given geometry $\mathbf{t}_P$ is a fixed matrix. However, as will be demonstrated, translating the position of the bead in the channel is equivalent to regenerating the entries of

Optics EXPRESS

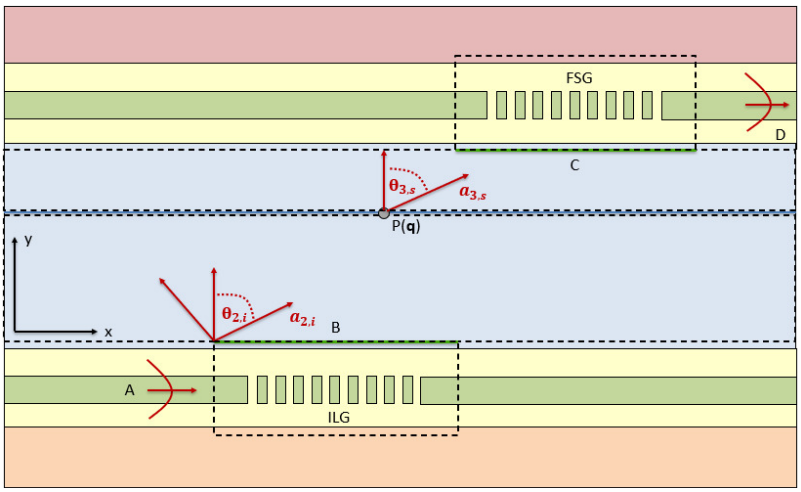

Fig. 9. TMM modularization of the dynamic system with a bead P at a position **q** in the channel. Modal coupling from A to D is calculated by cascading the ILG, microfludic channel, bead and FSG matrices resulting from this TMM modularization.

the $\mathbf{t}_{A\to P}$ and $\mathbf{t}_{P\to C}$ matrices, a simple and fast operation. As such, the transient transmission associated with the bead's passage through the channel (Fig. 3) can be efficiently simulated by iteratively solving Eqn.9) while updating the $\mathbf{t}_{A\to P}$ and $\mathbf{t}_{P\to C}$ matrices based on the bead's position. This enables the fast evaluation of a P2B for a given grating configuration leading to significantly more efficient optimizations. Performing the same computation using an FDTD would require simulating the entire system for each position of the bead as it propagates through the channel, resulting in computational overhead too large to feasibly use in an optimization loop. Consequently, the model enables the efficient optimization of transient P2B, a more meaningful Figure of Merit for cell detection compared to static power transmission.

3.2. *Polystyrene bead*

In order to facilitate the computation and optimiziation of a transient P2B, a coherent transmission matrix for the bead $\mathbf{t}_P$ must be incorporated into the TMM. In 2D modeling, the bead is treated as a lossless, dielectric cylinder infinite in z, whose scattered fields, when excited with a plane wave, can be computed using Mie Scattering theory. In our system, the free space wavelength $\lambda_0 = 638$ nm is comparable to the bead radius $R_{bead} = 3$ µm. As such, no Rayleigh approximations are applicable and Maxwell's equations must be solved in full for the correct physical boundary conditions using a scheme such as that described in [28]. In this work, the Python library Scatsol [29] is selected for this purpose. The fields are then used to calculate the transmission matrix of the bead $\mathbf{t}_P$ using the novel scheme described in Sec. 7 of Supplement 1. Assuming a bead with a circular symmetry, and using a spectrum of plane waves with equal angular spacing, only one row/column of $\mathbf{t}_P$ needs to be computed. The other rows/columns are simply shifted copies. The bead transmission matrix therefore only needs to be calculated once (for each bead diameter) and may be re-used within the TMM. The construction of a 2881 plane wave bead transmission matrix takes approximately 6 hours on the same computational hardware used elsewhere in this work. While this represents additional computational overhead, the matrix construction for a given bead geometry is a one-time calculation and isn't included in the TMM computation times.

In the TMM, the bead is abstracted to a point scattering matrix $\mathbf{t}_P$ unique to the bead geometry and refractive index. While this work primarily simulates a system where $R_{bead} = 3$ µm, the procedure described in Sec. 7 of Supplement 1 can be performed for a dielectric cylinder of

Optics EXPRESS

any radius to produce scattering matrices for beads of different sizes. For scattering objects with arbitrary, non cylindrical geometries, calculating the scattered fields due to a plane wave excitation might not be possible using analytical methods. In such cases the fields may be calculated using an FEM solver, then following a scheme similar to Sec. 7 in Supplement 1, may be used to construct a scattering matrix. However, for a non-symmetric bead it would become necessary to compute the scattered fields for every incident angle. $\mathbf{t}_P$ may be replaced with the transmission matrix for an arbitrary scattering object without effecting the grating matrices, $\mathbf{t}_{A->B}$ and $\mathbf{t}_{C->D}$ or the propagation matrices $\mathbf{t}_{B->P}$ and $\mathbf{t}_{P->C}$. Consequently, recalculating and replacing $\mathbf{t}_P$ is all that's necessary to simulate the transient P2B of any arbitrary scattering object passing through the channel. The TMM can then be used to simulate and optimize the system for the discrimination of highly aspherical cells.

3.3. Microfluidic channel

In the TMM, representing the bead as an abstract transmission matrix $\mathbf{t}_P$ collapses the spatial features of the bead into a point scattering object. Placing a bead in the channel replaces $\mathbf{t}_{B->C}$ with a matrix $\mathbf{t}_P$ governing the scattering of plane waves by the bead and two additional matrices $\mathbf{t}_{B->P}$ and $\mathbf{t}_{P->C}$ governing the propagation of plane waves from the ILG (B) to the bead (P) and the bead to the FSG (C) respectively. The phase rotations plane waves incur from channel propagation for a bead at position $\mathbf{q}$ are similarly calculated using Eqns. (10) and (11) based on Fig. 10. The phase rotations are then used to populate the transmission terms in the $\mathbf{t}_{B->P}$ and $\mathbf{t}_{P->C}$ matrices.

$$\phi_{2,i} = \mathbf{k_{2,i}} \cdot \mathbf{r_2} = \frac{2\pi n_w}{\lambda_0}\sqrt{x_2^2 + y_2^2}cos(\theta_{2,i} - \alpha_2) \tag{10}$$

$$\phi_{3,i} = \mathbf{k_{3,i}} \cdot \mathbf{r_3} = \frac{2\pi n_w}{\lambda_0}\sqrt{x_3^2 + y_3^2}cos(\theta_{3,i} - \alpha_3) \tag{11}$$

$$\mathbf{t}_{B\to P} = \begin{pmatrix} t_{B\to P}^{(1)} & \cdots & 0 \\ \vdots & \ddots & \vdots \\ 0 & \cdots & t_{B\to P}^{(N)} \end{pmatrix} \tag{12}$$

$$\mathbf{t}_{P\to C} = \begin{pmatrix} t_{P\to C}^{(1)} & \cdots & 0 \\ \vdots & \ddots & \vdots \\ 0 & \cdots & t_{P\to C}^{(N)} \end{pmatrix} \tag{13}$$

3.4. Model validation and benchmarking

Having calculated the transmission matrix $\mathbf{t}_P$ for a $R_{bead} = 3$ μm bead, the TMM can now be validated by comparing its performance against FDTD simulations. The matrices $\mathbf{t}_{A\to B}$ and $\mathbf{t}_{C\to D}$ were generated for gratings with $\Lambda_{ILG} = \Lambda_{FSG} = 0.49$ μm and 21 and 41 periods. Using Eqn. (9), power transmission through the dynamic system was calculated while sweeping the bead's x position in steps of 100 nm between -5 μm$<x_2<$20 μm and -5 μm$<x_2<$30 μm for the 21-period and 41-period gratings respectively, with the y position fixed at the mid-channel. This was performed for an FSG offset of $x_{FSG} = 3.1\ \mu m$ and a 2881 plane wave expansion.

Figure 11 shows the results of the simulations compared to those obtained via Lumerical FDTD. The results demonstrate excellent agreement between the TMM and FDTD for the 21-period grating configuration and good agreement for the 41-period configuration. For the 41-period grating, the baseline error between the TMM and FDTD appears to be 0.0108, close to the maximum static error of 0.0102 found in Fig. 7(b). Once again, the error is likely due to

Optics EXPRESS

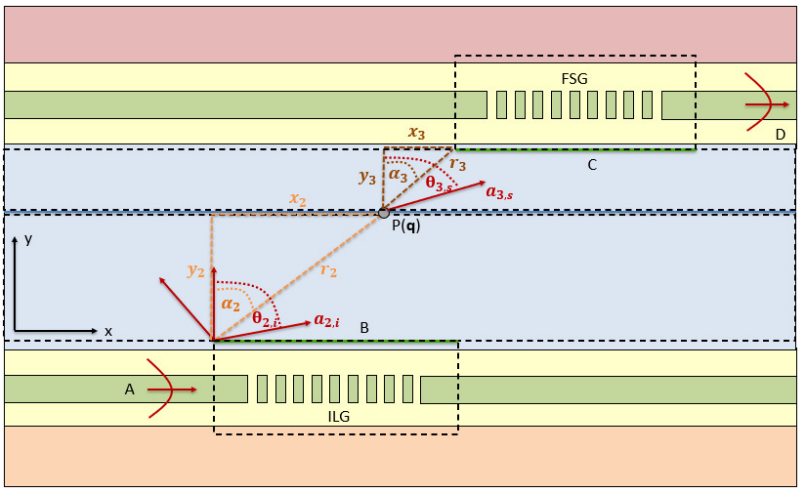

Fig. 10. System schematic depicting plane waves $a_{2,i}$ and $a_{3,s}$ with propagation angles $\theta_{2,i}$ and $\theta_{3,i}$ traversing distances r_2 (composed of x_2 and y_2) and r_3 (composed of x_3 and y_3) at angles α_2 and α_3. These parameters are used to determine the plane wave phase rotations by Eqn. (10) and (11) used to construct the channel transmission matrices in Eqns. (12) and (13).

inter-component reflection ignored by the TMM. However, the transients' shapes and their P2Bs are sufficiently similar to justify using the TMM for approximating the optimal 41-period grating configuration.

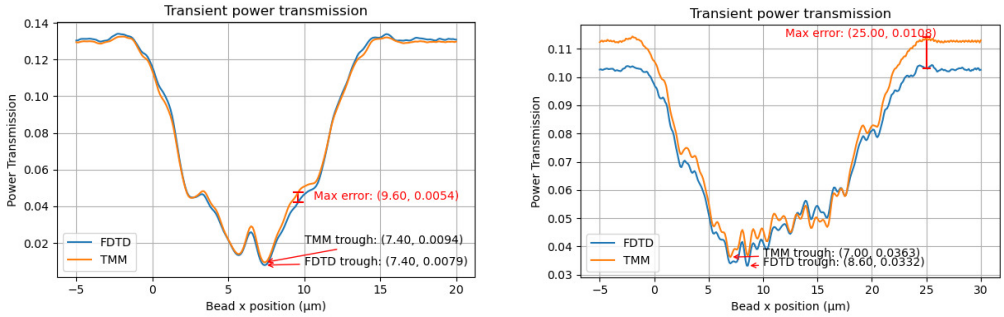

(a) Grating with 21 periods.

(b) Grating with 41 periods.

Fig. 11. Transient power transmission calculated while sweeping the bead position by both a 2881 plane wave TMM and Lumerical FDTD for gratings with $\Lambda_{ILG} = \Lambda_{FSG} = 0.49$; μm and $x_{FSG} = 3.1$ μm. The similar shape, trough position and small error indicate sufficiently close agreement between the TMM and FDTD simulations.

The computation times for the dynamic bead position sweeps in Fig. 11 are outlined in Table 2. An FDTD simulation adopting a mesh accuracy setting of 5 took, on average, 999 s to complete a single point in the bead position sweep for the 21-period grating configuration (see Fig. S14 of Supplement 1). Additionally, with a mesh accuracy setting of 8, a single point in the bead position sweep took an FDTD simulation on average 6881 s for the 41-period configuration (see Fig. S15 of Supplement 1). The averages for each grating configuration were multiplied by the number of sweep points to estimate the total FDTD computation time. Table 2 demonstrates a four to five order-of-magnitude improvement in computational efficiency using the TMM, which

Optics EXPRESS

becomes even more significant with finer bead position resolution sweeps. As such, it is now feasible to run an optimization algorithm on the grating configuration for maximum P2B within a reasonable time frame.

Table 2. Computation times of the dynamic sweeps in Fig. 11 performed on the same computational hardware.

Periods	Points in Sweep	Model	Computation Time (s)
21	251	FDTD	2.51×10^5
21	251	TMM	15
41	351	FDTD	2.41×10^6
41	351	TMM	53

3.5. Grid search

The benefits of the model's efficiency become evident when performing a P2B grid search (GS) for grating configurations with 20 periods, varying between 0.4 μm $\leq \Lambda_{ILG} = \Lambda_{FSG} \leq$ 0.6 μm in 200 increments of 1 nm, and FSG offsets between −5 μm $\leq x_{FSG} \leq$ 15 μm in 200 increments of 10 nm. An FSG offset increment of 10 nm, rather than 1 nm, is used to reduce the grid search completion time. For each grating configuration, x_2 is swept between −10 μm $\leq x_2 \leq$ 30 μm in steps of 100 nm with y_2 fixed mid-channel to compute the transient P2B. Figure 12(a) shows the results of this grid search. The maximum transient P2B of 0.1308, for the blue trace in in Fig. 12(b), is obtained with $\Lambda_{ILG} = \Lambda_{FSG} = 0.510$ μm and $x_{FSG} = 6.10$ μm.

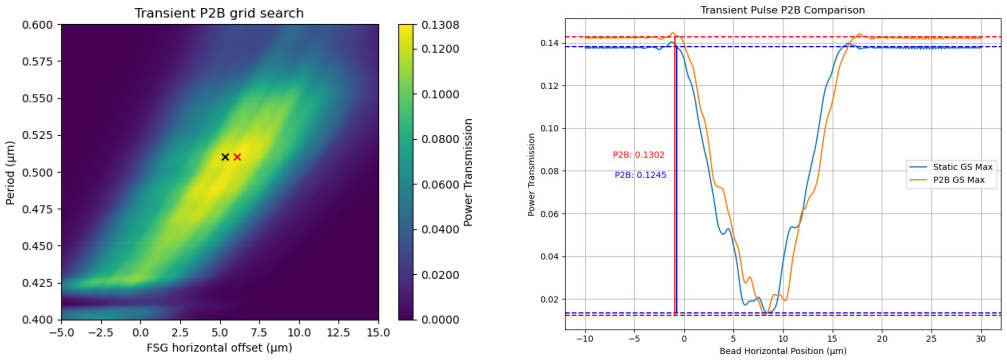

(a) (b)

Fig. 12. (a) P2B calculation, sweeping $\Lambda_{ILG} = \Lambda_{FSG}$ (with a 20-period grating) and the FSG horizontal offset x_{FSG}. The maximum transient $P2B = 0.1308$, depicted by the orange trace in (b), is obtained with $\Lambda_{ILG} = \Lambda_{FSG} = 0.510$ μm and $x_{FSG} = 6.10$ μm and indicated on the heat map (a) with a red cross. The optimum configuration found previously in Sec. 2.6 is indicated with a black cross in (a) and the blue trace in (b), demonstrating that the optimum configurations for a static and dynamic system are not equivalent.

Comparing the results of Fig. 12 with Fig. 8, there is a strong, albeit imperfect, correlation between P2B and static transmission. Notably, the grating configuration that yields the maximum static transmission is close but not identical to the configuration that yields the maximum P2B. The grid search took approximately 10 hours to simulate the P2B for $201 \times 201 = 40,401$ grating configurations with 10 nm interval FSG offset steps. For Lumerical FDTD to complete this same task on the same computing hardware, it would have taken approximately $40,401 \times 70$ hrs $\approx 2.83 \times 10^6$ hours, or 117,386 days, an impractically long period of time.

Optics EXPRESS

3.6. Bead y offset

The modeling so far has assumed that the bead propagates through the microfluidic channel with its y position fixed at the mid-channel. In reality, the bead may pass through the channel with a vertical offset, which can affect the profile of the transient and, consequently, the P2B. Indeed, in [11] inertial focusing directs the beads towards the top and bottom walls of the channel. The TMM allows us to efficiently evaluate the impact of a vertical offset, e.g., ±2 μm from the channel center, on the transient, as shown in Fig. 13(a), where we observe slight changes in the shape and position of the transient. Additionally, the TMM enables us to characterize the distribution of P2B for a range of bead vertical offsets, such as $-2\ \mu m < \Delta y < 2\ \mu m$ in 10 nm steps.

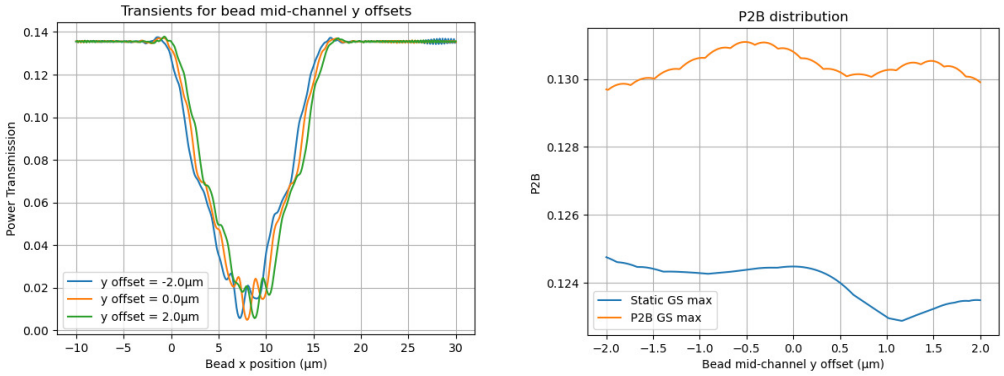

(a) (b)

Fig. 13. (a) Transients when the bead is offset in y from mid-channel by 0 μm, −2 μm and 2 μm for the grating configuration in Fig. 12. (b) Distribution of P2B for y offsets in 10 nm increments between −2 μm and 2 μm for the grating configurations in Figs. 8 and 12. The TMM enables efficient visualization and quantification of robustness for a certain grating configuration.

Figure 13(b) depicts such distributions for the grating configurations identified via GS in Figs. 8 and 12. From Fig. 13(b), we observe that the P2B distribution appears slightly tighter for the grating configuration shown in Fig. 12. The standard deviation of this distribution, $\sigma_{\mathbf{\Delta y}}$, quantifies the robustness of the grating configuration to bead vertical offset Δy and serves as an additional metric for evaluating the performance of a grating configuration. The values $\sigma_{\mathbf{\Delta y}} = 0.0006$ and $\sigma_{\mathbf{\Delta y}} = 0.0004$ for the grating configurations in Figs. 8 and 12, respectively, confirm our visual intuition. While it is possible to devise an optimization objective function that minimizes this standard deviation, thereby maximizing robustness, this work uses this metric to compare grating configurations post P2B optimization.

3.7. Bead size

The modeling so far has assumed that the bead representing a biological cell has a fixed radius of $R_{bead} = 3$ μm. In the TMM, the transmission matrix for a bead of a specific radius is generated only once (using the scheme described in Sec. 7 of Supplement 1) and then repeatedly used to simulate transients for different grating configurations. Similarly, the transmission matrix for a bead with a $R_{bead} = 4.5$ μm radius can be generated and replace the $R_{bead} = 3$ μm matrix, allowing the TMM to quickly simulate the impact of varying bead sizes on the transient and P2B, as shown in Fig. 14. The difference in P2B magnitude for cells of different sizes $\Delta P2B_{\Delta R}$ serves as an additional metric for evaluating the performance of a grating configuration. A grating configuration that yields a larger difference in P2B for different cell sizes is better suited for discriminating between various types of cells.

Optics EXPRESS

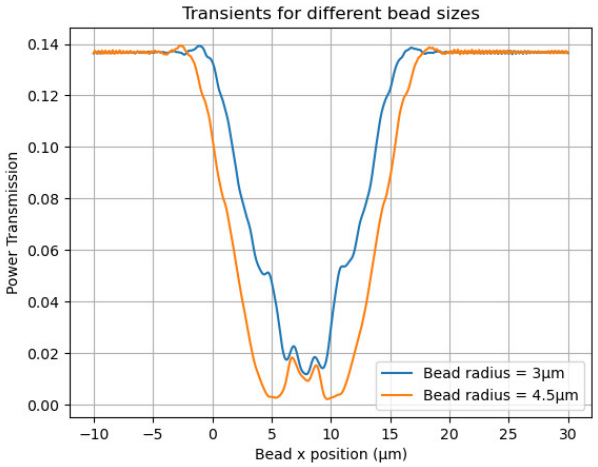

Fig. 14. Transients for beads of different sizes for the grating configuration in Fig. 12. The difference in P2B of such transients is another optimizable metric enabled by the TMM.

Since the purpose of forward scattering is to measure and distinguish between cells of different sizes, this is a particularly valuable metric in flow cytometry. While it is possible to incorporate the P2B difference into an objective function for optimization, this work uses it as an additional metric to further to compare grating configurations post-P2B optimization.

4. Optimization

4.1. Outline

With an accurate and computationally efficient means of modeling transients, we may now optimize the grating configuration so as to maximise the P2B. We investigate 2 grating parameterizations in this work, a uniform period and fill grating and an apodized grating where period and fill are varied linearly along the length of the grating. For a uniform grating, the period, period count and FSG offset x_{FSG} are optimizable parameters. It is possible to perform an exhaustive grid search of an integer period count between 20 and 40, 200 increments of 1 nm of the period between $0.4\ \mu\text{m} \leq \Lambda_{ILG} = \Lambda_{FSG} \leq 0.6\ \mu\text{m}$, and 2000 increments of 1 nm of the FSG offset between $-5\ \text{m} \leq x_{FSG} \leq 15\ \mu\text{m}$. However, based on the 10 hours required to complete the grid search depicted in Fig. 12(a), increasing the resolution by a factor of 10 and incorporating 21 different period numbers would take over $10\,\text{hrs} \times 10 \times 21 = 2100\,\text{hrs}$, or 84 days. Additionally, this work employs a linearly apodized grating parameterization detailed in Sec. 8.B. of Supplement 1 which is a modified version of the strategy described in [30]. This approach introduces linear apodization strength as an additional optimizable variable. With three continuous and one discrete variable, the dimensionality of the search space becomes too high for a grid search to be feasible. Therefore, an optimization algorithm is required to efficiently explore the parameter space. The optimization problem is classified in more detail in Sec. 9.A of Supplement 1.

Genetic and Particle Swarm Optimization algorithms have been historically used in grating coupler optimization and perform well even in higher-dimensional parameter spaces [18,31–33]. However, these algorithms require multiple objective function evaluations for each population or swarm iteration, leading to significant computational overhead and time-consuming optimization runs. Additionally, both algorithms' update rules involve several tunable hyperparameters and stochastic terms, which can cause the population or swarm to prematurely converge on a local rather than a global maximum due to semi-stochastic updates or suboptimal hyperparameter settings. While the hyperparameters can be adjusted to favor exploitation or exploration, ensuring

Optics EXPRESS

convergence to a global optimum, the best settings for a particular optimization problem are not always known a priori. Performing multiple computationally expensive optimization runs to fine-tune these hyperparameters further compounds the computational overhead.

Bayesian Optimization using Gaussian Processes is an optimization technique that leverages a probabilistic model to efficiently predict and explore different parameter sets, described in more detail in Sec. 9.B of Supplement 1. BO has more recently been used in the optimization of grating couplers [34–36] and demonstrated an order-of-magnitude reduction in objective function evaluations compared to other algorithms in photonic device optimization [24]. In this work, the computational efficiency of BO is used to conduct a sweep across different integer numbers of grating periods. Grating period counts within a relatively small range are explored, specifically from 20 to 40, and for each integer value, BO is used to search for the optimal continuous grating parameters, such as period and FSG offset. Although methods exist to accommodate integer parameters within BO algorithms [37], this work takes advantage of the low dimensionality of the parameterization and the narrow range of period counts to perform a more exhaustive search. A Gaussian Process with a Matérn 5/2 kernel and an expected improvement acquisition function are used in the BO eliminating the need for tunable hyperparameters. Each BO consisted of 10 initialization and 100 training samples.

4.2. Results

Table 3 outlines optimum grating configurations for the uniform (ID 3 in Table 3) and apodized (ID 4) parameterizations compared to the best result found by a grid search (GS) of the static transmissions (ID 1) from Sec. 2.6 and P2B's (ID 2) from Sec. 3.5. The optimization results are outlined in detail in Sec. 10 of Supplement 1. A GS of BO's for a uniform grating parameterization (ID 3) yields a P2B of 0.1389 as in Fig. 15, a modest 0.26 dB increase on the result found by a GS of P2B (ID 2). The result was substantially improved with an apodized grating parameterization (ID 4) achieving a P2B of 0.221 as in Fig. 15, a 2.02 dB P2B improvement on the optimum obtained via a uniform grating parameterization (ID 3). Furthermore, this grating configuration represents a 2.49 dB improvement on the grating configuration found using a GS of uniform grating parameters to maximise static transmission (ID 1). All grating configurations are highly robust to variance in the vertical offset of the bead $\sigma_{\Delta y}$, with only small differences in $\sigma_{\Delta y}$ found between grating configurations. The apodized grating (ID 4) yields the largest $\Delta P2B_{\Delta R}$ at 0.0213. This is a 1.92 dB improvement on the next best configuration (ID 3), making the apodized grating best placed to discriminate between beads of radii $R_{bead} = 3$ µm and $R_{bead} = 4.5$ µm.

Table 3. Grid search (GS) and Bayesian Optimization (BO) results. For uniform grating parameterisations, the apodization entry is left blank to indicate no apodization.

ID	Type	Period Count	Period (nm)	FSG Offset (μm)	Apodization ($1/\mu m$)	P2B	$\sigma_{\Delta y}$	$\Delta P2B_{\Delta R}$
1	GS	20	510	5.30		0.1245	0.0006	0.0105
2	GS	20	510	6.10		0.1308	0.0004	0.0049
3	GS + BO	24	511	5.323		0.1389	0.0003	0.0137
4	GS + BO	39	423	−3.959	0.0135	0.2210	0.0003	0.0213

Optics EXPRESS

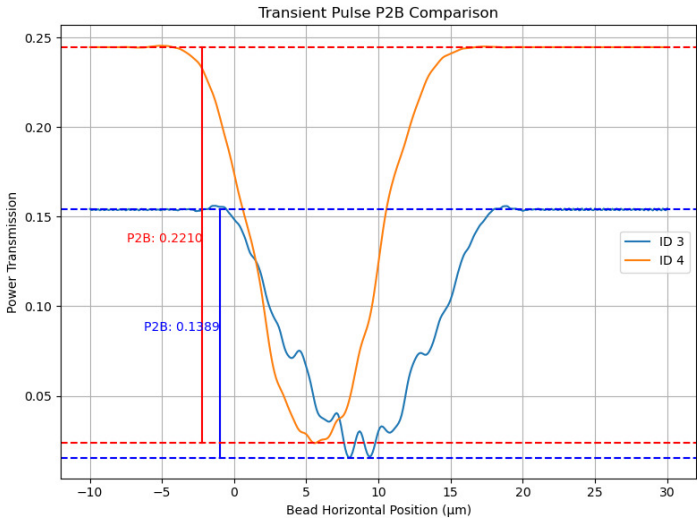

Fig. 15. Transient and P2B of the uniform (ID 3) and apodized (ID 4) grating configurations found via GS of BO's in Table 3. The apodized grating (ID 4) is the best result found in this work, showing a 2.02dB improvement over the uniform grating (ID 3).

5. Discussion

This work successfully developed and validated a 2D TMM to simulate static and transient transmission in a microfluidic grating system, achieving a computation speed four to five orders-of-magnitude faster than an FDTD solver. The TMM's computational efficiency enabled the fast simulation of effects that are computationally prohibitive to model with an FDTD solver, particularly the impact of variations in the bead's y position and size on the transient. The model was further employed in a series of grid searches and Bayesian optimizations to efficiently tune both uniform and apodized grating parameters, maximizing the transient P2B. An initial result (see Fig. 8) was obtained by a grid search of uniform grating configurations in a static system model, a similar approach to [11], but using the proposed TMM instead of FDTD simulations. Progressive refinements in modeling, optimization approach, and grating parameterization each demonstrated an improvement in P2B and the final apodized grating configuration, optimized for a dynamic system, delivered a 2.49 dB improvement in P2B over the initial result. The results illustrate the effectiveness of this approach for enhancing transient pulse characteristics in microfluidic systems.

While this work demonstrated a number of the TMM's aspects and capabilities there are several ways these could be expanded on in future work. One potential direction is incorporating the area between the transient and baseline as an additional metric, which is commonly used in flow cytometry. Although not the focus of this work, this area could easily be included in a new objective function, allowing the grating configuration to be optimized for maximum area instead of P2B without any additional computational cost. Furthermore, metrics such as $\Delta P2B_{\Delta R}$ and $\sigma_{\Delta y}$ could be integrated into a multi-objective function or robust optimization method.

Extending the model to 3D, by accounting for the z variation in grating geometry and modeling the bead as a dielectric sphere, would enable simulations of effects like polarization mixing, thus improving accuracy. Although this would increase computational cost, the efficiency gain compared to a 3D FDTD solver would still be substantial.

Optics EXPRESS

While this work focused on uniform and linearly apodized parameterizations, future studies could explore non-linear apodizations or optimize individual grating teeth widths within the optimization loops to better shape the radiated field profile and enhance the transient P2B.

Simulating and optimizing additional collector gratings, such as the Side Scattering Grating described in [11] that collects light that has been scattered by the bead, is also feasible with the TMM. A process similar to that used for the FSG can be applied to construct a transmission matrix for the Side Scattering Grating, which can then replace the FSG in the TMM. This additional TMM can be employed to optimise an alternative P2B objective function, where minimal baseline and maximal peak is desirable. This new objective configuration can be incorporated into a multi-objective function for the simultaneous optimization of the Forward and Side Scattering Gratings.

In this work, the microfluidic channel was approximated as a static, homogeneous medium. In reality, the bead is propelled through the channel by dynamic, microfluidic effects described in [11] that would disturb the uniformity of the dielectric profile. Future work could model effects such as turbulence as randomized noise in the channel transmission matrices $\mathbf{t}_{B->P}$ and $\mathbf{t}_{P->C}$. Several transients may be efficiently simulated in a turbulent channel to evaluate an average P2B which may then be incorporated into an objective function.

The mathematical operations in this work were performed using the standard Python library, NumPy. While matrix operations are fast (NumPy uses optimized C libraries under the hood), Python is an interpreted language, so its execution is generally slower compared to a compiled language like C. Future work could streamline larger optimizations by pre-calculating matrices for lookup tables or using a just-in-time compiler like Numba [38] for key operations to reduce the computational overhead of Python. Finally, while the system concept was experimentally demonstrated in [11], future work could fabricate and experimentally characterize the optimized design presented in this work.

Disclosures. The authors declare no conflicts of interest.

Data availability. Data underlying the results presented in this paper are not publicly available at this time but may be obtained from the authors upon reasonable request.

Supplemental document. See Supplement 1 for supporting content.

References

1. A. B. Shrirao, Z. Fritz, E. M. Novik, *et al.*, "Microfluidic flow cytometry: The role of microfabrication methodologies, performance and functional specification," Technol. (Singapore World Sci.) **6**(1), 1–23 (2018). Epub 2018 Mar 16.
2. N.-T. Huang, H.-l. Zhang, M.-T. Chung, *et al.*, "Recent advancements in optofluidics-based single-cell analysis: optical on-chip cellular manipulation, treatment, and property detection," Lab Chip **14**(7), 1230–1245 (2014).
3. B. Jiang, H. Dai, Y. Zou, *et al.*, "Continuous detection of micro-particles by fiber bragg grating fabry-perot flow cytometer," Opt. Express **26**(10), 12579–12584 (2018).
4. A. Zhukov, R. Pritchard, M. Withers, *et al.*, "Extremely high-throughput parallel microfluidic vortex-actuated cell sorting," Micromachines (Basel) **12**(4), 389 (2021).
5. P. Friis, K. Hoppe, O. Leistiko, *et al.*, "Monolithic integration of microfluidic channels and optical waveguides in silica on silicon," Appl. Opt. **40**(34), 6246 (2001).
6. B. R. Watts, Z. Zhang, C. Q. Xu, *et al.*, "A photonic-microfluidic integrated device for reliable fluorescence detection and counting," Electrophoresis **33**(21), 3236–3244 (2012).
7. J. T. Butement, P. M. Holloway, N. A. Englyst, *et al.*, "Integrated optical waveguides and inertial focussing microfluidics in silica for microflow cytometry applications," J. Micromech. Microeng. **26**(10), 105004 (2016).
8. S. Kerman, D. Vercruysse, T. Claes, *et al.*, "Integrated nanophotonic excitation and detection of fluorescent microparticles," ACS Photonics **4**(8), 1937–1944 (2017).
9. J. T. Butement, P. M. Holloway, J. A. Welsh, *et al.*, "Monolithically-integrated cytometer for measuring particle diameter in the extracellular vesicle size range using multi-angle scattering," Lab Chip **20**(7), 1267–1280 (2020).
10. T. Hong, D. Li, and J. G. Valentine, "Metasurface-enabled barcoding for compact flow cytometry," Optica **11**(4), 577–582 (2024).
11. S. Jooken, K. Zinoviev, G. Yurtsever, *et al.*, "On-chip flow cytometer using integrated photonics for the detection of human leukocytes," Sci. Rep. **14**(1), 10921 (2024).
12. L. Cheng, S. Mao, Z. Li, *et al.*, "Grating couplers on silicon photonics: Design principles, emerging trends and practical issues," Micromachines **11**(7), 666 (2020).

Optics EXPRESS

13. C. C. Stewart, S. J. Stewart, and R. C. Habbersett, "Resolving leukocytes using axial light loss," Cytometry **10**(4), 426–432 (1989).
14. M. Sheetz and H. Yu, *The Cell as a Machine*, Cambridge Texts in Biomedical Engineering (Cambridge University Press, 2018).
15. N. Caille, O. Thoumine, Y. Tardy, *et al.*, "Contribution of the nucleus to the mechanical properties of endothelial cells," J. Biomech. **35**(2), 177–187 (2002).
16. R. E. Waugh, E. Lomakina, A. Amitrano, *et al.*, "Activation effects on the physical characteristics of t lymphocytes," Front. Bioeng. Biotechnol. **11**, 1175570 (2023).
17. Y. Zhang, D. Kwong, X. Xu, *et al.*, "On-chip intra- and inter-layer grating couplers for three-dimensional integration of silicon photonics," Appl. Phys. Lett. **102**(21), 211109 (2013).
18. M. Sodagar, R. Pourabolghasem, A. A. Eftekhar, *et al.*, "High-efficiency and wideband interlayer grating couplers in multilayer si/sio2/sin platform for 3d integration of optical functionalities," Opt. Express **22**(14), 16767–16777 (2014).
19. L. Christopher Lalau-Keraly, "Lumopt: Easy adjoint optimization for lumerical," (2018). Accessed: 2024.
20. A. Michaels and E. Yablonovitch, "Inverse design of near unity efficiency perfectly vertical grating couplers," Opt. Express **26**(4), 4766–4779 (2018).
21. T. V. Vaerenbergh, P. Sun, S. Hooten, *et al.*, "Wafer-level testing of inverse-designed and adjoint-inspired vertical grating coupler designs compatible with duv lithography," Opt. Express **29**(23), 37021–37036 (2021).
22. A. M. Hammond, J. B. Slaby, M. J. Probst, *et al.*, "Multi-layer inverse design of vertical grating couplers for high-density, commercial foundry interconnects," Opt. Express **30**(17), 31058–31072 (2022).
23. M. Yang, Y. Yan, Z. Wu, *et al.*, "High-performance grating couplers on 220-nm thick silicon by inverse design for perfectly vertical coupling," Sci. Rep. **13**(1), 18112 (2023). ID: Yang2023.
24. P.-I. Schneider, X. Garcia Santiago, V. Soltwisch, *et al.*, "Benchmarking five global optimization approaches for nano-optical shape optimization and parameter reconstruction," ACS Photonics **6**(11), 2726–2733 (2019).
25. J. W. Goodman, *Introduction to Fourier Optics* (Roberts & Co. Publishers, 2005), 3rd ed.
26. B. E. A. Saleh and M. C. Teich, *Fundamentals of Photonics*; 3rd ed., Wiley series in pure and applied optics (Wiley, 2019).
27. P. Bienstmann, "Camfr: Cavity modelling framework," (2017). Accessed: 2024.
28. C. Balanis, *Advanced Engineering Electromagnetics*, CourseSmart Series (Wiley, 2012).
29. tiagovla, "2d analyitcal solver for cylinderical dielectrics," https://github.com/tiagovla/scatsol.
30. R. Marchetti, C. Lacava, A. Khokhar, *et al.*, "High-efficiency grating-couplers: Demonstration of a new design strategy," Sci. Rep. **7**(1), 16670 (2017).
31. D. Taillaert, P. Bienstman, and R. Baets, "Compact efficient broadband grating coupler for silicon-on-insulator waveguides," Opt. Lett. **29**(23), 2749–2751 (2004).
32. B. Wohlfeil, L. Zimmermann, and K. Petermann, "Optimization of fiber grating couplers on soi using advanced search algorithms," Opt. Lett. **39**(11), 3201–3203 (2014).
33. A. Bozzola, L. Carroll, D. Gerace, *et al.*, "Optimising apodized grating couplers in a pure soi platform to −0.5 db coupling efficiency," Opt. Express **23**(12), 16289–16304 (2015).
34. Y. Zhao, F. Yang, J. Song, *et al.*, "Bayesian-optimized infrared grating for tailoring thermal emission to boost thermophotovoltaic performance," J. Appl. Phys. **133**(12), 124904 (2023).
35. P. Manfredi, A. Waqas, and D. Melati, "Stochastic and multi-objective design of photonic devices with machine learning," Sci. Rep. **14**(1), 7162 (2024).
36. Y. Miyatake, N. Sekine, K. Toprasertpong, *et al.*, "Computational design of efficient grating couplers using artificial intelligence," Jpn. J. Appl. Phys. **59**(SG), SGGE09 (2020).
37. E. C. Garrido-Merchán and D. Hernández-Lobato, "Dealing with categorical and integer-valued variables in bayesian optimization with gaussian processes," Neurocomputing **380**, 20–35 (2020).
38. N. D. Team, "Numba: A high performance python compiler," https://numba.pydata.org/ (2023). Accessed: 2024-09-09.

157.192.248.247 {3025-03-30 04:20}